Unravelling the evolution of an Alpine to post-glacially active fault in the Swiss Alps

Michaela Ustaszewski [a],*, Marco Herwegh [a], Alastair F. McClymont [b],
O. Adrian Pfiffner [a], Robyn Pickering [a], Frank Preusser [a]

[a] *Institute of Geological Sciences, University of Bern, Baltzerstrasse 1-3, 3012 Bern, Switzerland*
[b] *Institute of Geophysics, Swiss Federal Institute of Technology, Hönggerberg, 8093 Zürich, Switzerland*

Abstract

The Gemmi fault is a prominent NW–SE striking lineament that crosses the Gemmi Pass in the central Swiss Alps. A multidisciplinary investigation of this structure that included geological mapping, joint profiling, cathodoluminescence and scanning electron microscopy, stable isotope measurements, luminescence- and U-TH-dating, 3D ground penetrating radar (GPR) surveying and trenching reveals a history of fault movements from the Miocene to the Holocene. The main fault zone comprises a 0.5–3 m thick calcite cataclasite formed during several cycles of veining and brittle deformation. Displaced Cretaceous rock layers show an apparent dextral slip of ~ 10 m along the fault.

A detailed study of a small sediment-filled depression that crosses the fault provides evidence for a post-glacial reactivation of the fault. A trench excavated across the fault exposed a Late-Glacial-age loess layer and late Holocene colluvial-like slope-wash deposits that showed evidence for fault displacement of a few centimeters, indicating a recent strike-slip reactivation of the fault. Focal mechanisms of recent instrumentally recorded earthquakes are consistent with our findings that show that the fault at the Gemmi Pass, together with other parallel faults in this area, may be reactivated in today's stress field. Taking together all the observations of its ancient and recent activity, the Gemmi fault can be viewed as a window through geological space and time.
© 2007 Elsevier Ltd. All rights reserved.

Keywords: Swiss Alps; Neotectonics; Active faulting; Fault dating; Brittle reactivation; Fluid flow in faults

1. Introduction

In the central Alps, the collision of the Adriatic and the European continental margins initiated crustal thickening during the Cenozoic (Schmid et al., 1997; Escher et al., 1997; Pfiffner et al., 2002). GPS measurements show that the convergence of the two plates is ongoing at a rate of <2 mm/year (Calais et al., 2002), which is likely to have caused recent rock uplift and seismicity (Sue and Tricart, 2003; Persaud and Pfiffner, 2004; Ustaszewski and Pfiffner, in press).

The Alps have been studied for over 150 years and their evolution has been recorded in great detail (e.g. Trümpy, 1998, 2003; Pfiffner et al., 1997). In contrast, little is known about their recent history. This is surprising, because active and potentially seismogenic faults represent a significant hazard to life and constructions. Knowledge of their neotectonic history (<15 ka) is therefore a key issue and a pre-requisite for any assessment of seismic hazard.

Few previous researchers have touched on the topic of recent tectonic activity in the Alps. High-precision levelling measurements have been conducted since 1917 (Kahle et al., 1997; Funk and Gubler, 1980; Gubler et al., 1981; Schlatter and Marti, 2002), and the Swiss Seismologic Survey publishes an annual report of the seismic activity in Switzerland (e.g. Baer et al., 2005; Deichmann et al., 2006). Today's stress regime, inferred from focal mechanisms of instrumentally recorded earthquakes shows a contrast between the Penninic units south of the Rhône river, where N–S extension

---

* Corresponding author. Tel.: +41 31 631 4832; fax: +41 31 631 4843.
E-mail address: michaela.ustaszewski@geo.unibe.ch (M. Ustaszewski).

predominates, and the Helvetic units north of the Rhône river, which are characterised by a dextral strike-slip regime with an NW−SE oriented σ_1-axis and an NE−SW oriented σ_3-axis (Maurer and Deichmann, 1995; Maurer et al., 1997; Deichmann et al., 2002; Kastrup et al., 2004).

Sue (1998) identified an active fault in the Western Alps (Briançonnais Alps). Delacou et al. (2005) investigated large earthquakes in the Chablais area (south of Lake Geneva), and found a correlation between their focal mechanisms and known fault systems in the region. Neotectonic activity in eastern Switzerland was studied by Persaud (2002) and Persaud and Pfiffner (2004), and in western and central Swiss Alps by Ustaszewski (2007) and Ustaszewski and Pfiffner (in press). Several authors (Eckardt et al., 1983; Jäckli, 1965; Renner, 1982) have studied post-glacially active faults in the central Swiss Alps. Persaud and Pfiffner (2004) showed that a gravitational component plays an important role in the reactivation of these faults, whereas Ustaszewski and Pfiffner (in press) and Ustaszewski et al (in press) attributed a more complex interplay of differential uplift, large-scale gravitational movements and presumably also crustal tectonics in the formation of these faults.

Active faults often exhibit very subtle morphologic expressions of neotectonic deformation, which could be missed by a standard geological mapping survey. In tectonically quiescent terrains like the Alps, interdisciplinary approaches that investigate neotectonic faults in more detail, become a necessary alternative.

In this study, aerial photographs of the central and western Swiss Alps were searched for linear features as a first step to finding potentially post-glacially active faults. A number of these lineaments were subsequently visited in the field to assess their origin. Three different types of lineaments were distinguished: (a) lineaments caused purely by tectonic processes, (b) lineaments caused purely by gravitational processes, and (c) composite lineaments caused by gravitational and tectonic processes (Ustaszewski et al., in press).

To determine the age of past activity of the purely tectonic lineaments, indicative surface expression, morphology and especially deformation of the surrounding Quaternary sediments were studied. Few purely tectonic faults indicated post-glacial movements (Ustaszewski and Pfiffner, in press). In the course of these investigations, one fault showing unequivocal evidence for post-glacial activity was detected in the Gemmi Pass area (Fig. 1).

The aim of this study was to document and understand the evolution of the fault from Alpine time (Tertiary) to the present. In this sense, the geometry of the fault and its fabric from the kilometer down to the micrometer scale, and the timing of different deformation episodes were investigated in detail with a multidisciplinary approach that encompassed 3D ground penetrating radar (GPR), trenching, qualitative fabric analysis using cathodoluminescence microscopy and scanning electron microscopy, stable isotope measurements, and age determination (U−Th-dating and optically stimulated luminescence dating). This approach allowed us to unravel the complete structural record starting from: (i) the first initiation of the fault, (ii) later repetitive overprints by brittle deformation and fluid flow, to (iii) recent activity.

2. Geological setting

The lineament studied is a prominent NW−SE striking vertical fault located at the Gemmi Pass near Leukerbad in the Canton Valais (Figs. 1 and 2). The fault is oriented 225/90 and is perpendicular to the regional NE−SW striking fold axes. It can be followed over a horizontal distance of 2.6 km (probably 3.6 km as parts might be covered by slope talus) and an altitude range of 1800−2700 m. The fault cuts through the Helvetic nappe stack, which in this area consists of the Doldenhorn, the Gellihorn and the Wildhorn nappe. The affected rock types are Jurassic to Eocene carbonates, sandstones and shales (Pfiffner, 1993) that were thrusted and folded during Oligocene−Miocene times (Pfiffner et al., 2002). The fault investigated, hereafter referred to as ''Gemmi fault'', belongs to a regional-scale array of parallel faults, showing a spacing of several tens to a few hundred meters (Fig. 1a). The location of the Gemmi fault at the bottom of a large high-elevation valley suggests that the fault is unlikely to have been gravitationally reactivated. The fault is located close to the village of Leukerbad, where thermal springs show temperatures of up to 51 °C (Muralt and Vuataz, 1993). The absence of tritium in the pure thermal water component indicates that the water must have a long underground residence time of at least 50 years (Muralt and Vuataz, 1993; Huon et al., 1994). A Tertiary hydrothermal−telemagmatic dyke is reported at the Trubelnstock, 3 km south of the Gemmi fault (Furrer and Hügi, 1952), suggesting that elevated geothermal gradients have been present since that time.

3. Fault expression in bedrock

3.1. Characterisation of the fault zone

The fault exhibits a pronounced geomorphologic expression marked by a broad and, in places, pronounced ($\sim$3 m) incision in the landscape (Fig. 2a and b). It cuts through predominantly Jurassic to Eocene limestone and, in a few places, sandstone beds. The fault zone has a $\sim$20 m wide damage zone and the core zone itself varies in width between 0.5 m and 3 m (Fig. 3a). By following a weakly preserved lineation on the fault plane (fault plane: 250/55, striation: 335/05), an apparent dextral displacement of $\sim$10 m can be calculated from the offset host rock layers (bedding: $\sim$305/12). This is a minimum estimate of the slip along the fault since its initiation, because multiple reactivations of the fault with changing sense of slip cannot be ruled out. The offset along the fault is too small to be observed in the aerial photograph of Fig. 1b.

The host rocks are incorporated into the edges of the damage zone, where the limestones exhibit a cataclastic texture with white calcitic veins. The latter become more abundant towards the centre of the fault zone (Fig. 3b and e). The core zone is dominated by white cataclasite consisting of broken calcite joint filling. In those parts of the damage zone that
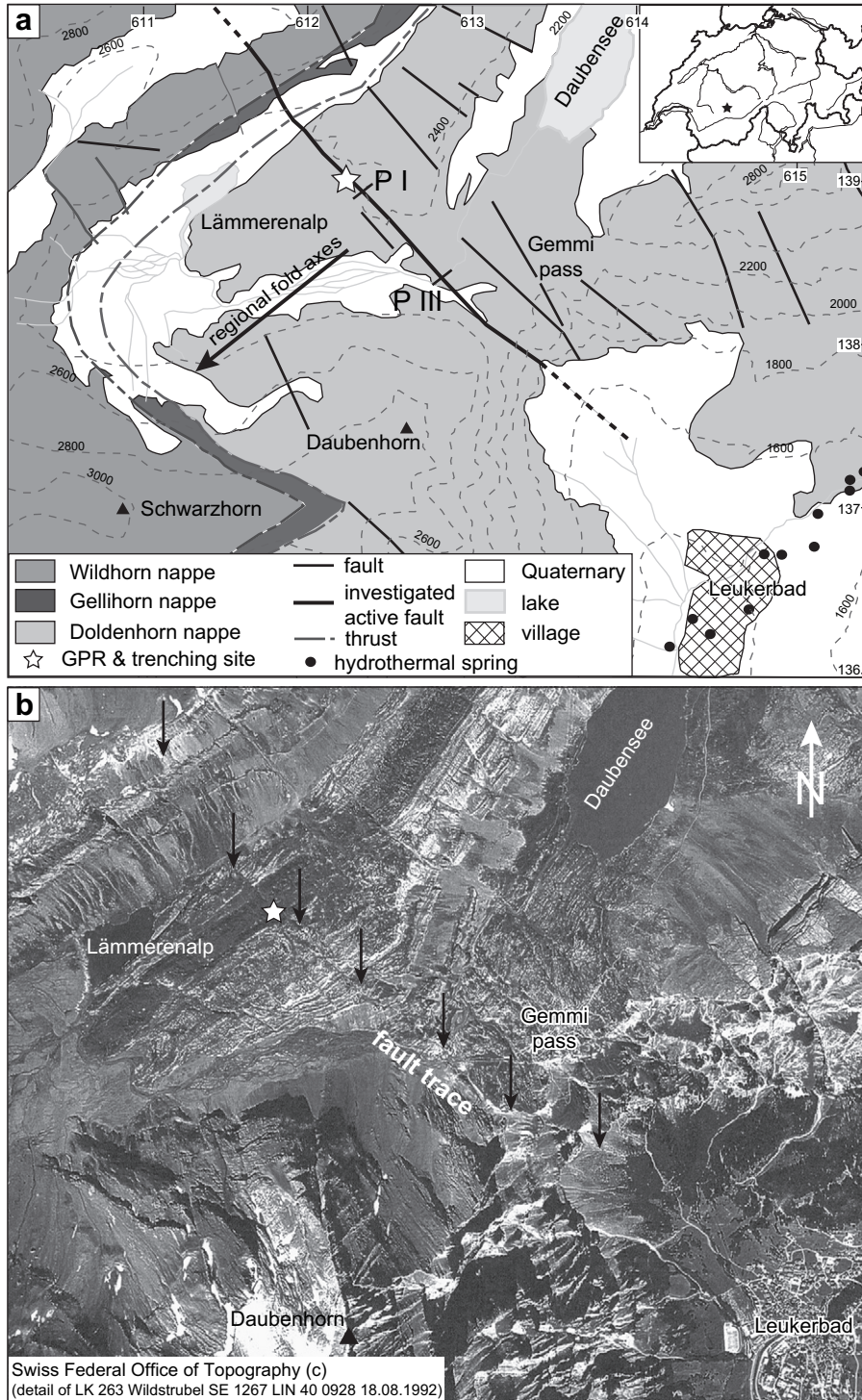
Fig. 1. (a) Overview map of the study area, geological units after Furrer et al. (1956). Location of joint profiles PI and PIII of Fig. 3 and GPR and trenching location of Fig. 7 are indicated. Coordinate numbers correspond to the Swiss national km grid. (b) Non-rectified aerial photograph of approximately the same area as in Fig. 1a. Arrows show the distinctive fault trace of the Gemmi fault.

have not undergone extensive brittle deformation, large calcite rhombohedra, with side lengths of up to 10 cm, are observed together with idiomorphic calcite crystals in open fissures (Figs. 3b—d).

Joints are pervasive throughout the entire bedrock, forming a dense, parallel and predominantly NW—SE oriented pattern (see rose diagrams in Fig. 3a). Joint density measurements

revealed an increasing density of fault parallel joints towards the main deformation zone, indicating a concentration of deformation towards the centre of the fault zone (Fig. 3a and b). Closed, open and reactivated joints were recorded in two ~40 m long profiles across the fault zone. Open and reactivated joints appear in a broad 15—20 m wide damage zone (Fig. 3a). The core zone itself is characterised by a very low
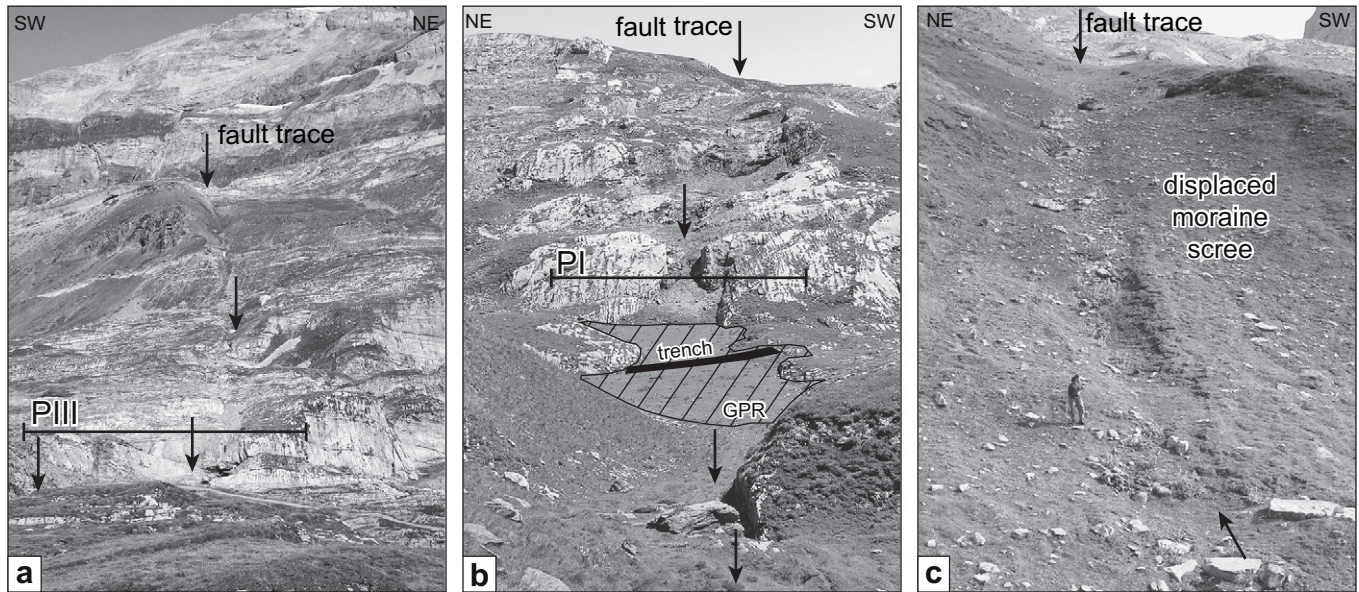
Fig. 2. (a) Overview photograph of the Gemmi fault (indicated by black arrows), showing its pronounced morphologic expression. Location of joint profile PIII of Fig. 3 is indicated. (b) Overview photograph of the Gemmi fault (indicated by black arrows). Locations of joint profile PI of Fig. 3, GPR-survey area (Fig. 7c) and trenching site (Fig. 7a and b) are indicated. (c) Subtle micromorphological observations along the Gemmi fault. Here, the fault trace crosses a slope and is discernible within displaced moraine scree.

number of visible joints. This anomaly is caused by worsening outcrop conditions and debris cover because of the strong disintegration of the fault rock.

3.2. Different generations of veins and cataclasite

Thin sections of the fault rock and the joints were investigated using cathodoluminescence microscopy in order to characterise the different phases of fluid flow and brittle reactivation of the fault zone. Variations in cathodoluminescence colours and intensities represent variations in the amounts of Mn and Fe, provoking and quenching cathodoluminescence, respectively. These different cathodo-microfacies allow us to decipher the geologic evolution of the sample, in particular, the interaction of brittle deformation, fluid flow and calcite precipitation.

Repetitive cycles of fluid flow and brittle reactivation of the fault zone can be discriminated by cross-cutting relationships and variations in cathodo-microfacies, where older generations generally appear in darker colours than the younger generations (Fig. 4a and b). The samples of the fault rock display at least six phases of fluid flow and brittle reactivation, four of them are shown in Fig. 4a.

A representative sample taken from the centre of the fault zone can be subdivided using textural criteria into three zones that parallel the fault plane (zones 1, 2 and 3 in Fig. 5a). Zone 1 is the oldest and comprises a proto-cataclasite with clasts of calcite crystals as large as 6 cm in a fine-grained calcitic matrix, forming a component-supported fabric. This zone reveals abundant brown-red, iron-rich solution seams. Zone 2 consists of <1 cm large clasts embedded in a layered gouge-matrix (Fig. 5b and c). These clasts are composed of fine-grained cataclastic material and are rimmed by partly idiomorphic

calcite crystals forming circumgranular crust cements and, in places, pendant seams. The matrix consists of fine-grained calcite with a grain size varying from 5 μm to 0.5 mm. Scanning electron microscopy (SEM) measurements of the matrix show a homogenous composition of almost 100% calcite. Trace concentrations of Mg were found in just a few locations. Bands of partly idiomorphic calcite crystals, with growth-directions towards the fault plane, pervade the matrix and have spacings of ∼1 mm. Zone 3 is closest to the fault plane and contains a component-supported proto-cataclasite with few voids, where calcite crystals grew into an open fissure. Cataclasite clasts in this zone are as large as 1 cm.

3.3. UV-light investigations

Observations of the sample under ultra-violet light revealed a greenish luminescence of zone 2 in Fig. 5. An investigation for biomarkers uncovered only recent organic material, precluding the action of micro-organisms in the formation of the layering in the fault gouge. Therefore, microbiological activity during the formation of zone 2 is unlikely (V. Thiele and J. Reitner, University of Göttingen, Germany, personal communication). A possible explanation for the luminescence is that organic material, originating from nearby black shales, was infiltrated into the fault zone by fluids.

3.4. Calcite twins

The nature of calcite twins gives information about the temperature conditions during their formation (Burkhard, 1993). Calcite grains of zone 1 are dominated by curved thick twins and twinned twins of type III, indicating formation temperatures of >200 °C and intense deformation. In zone 2, the
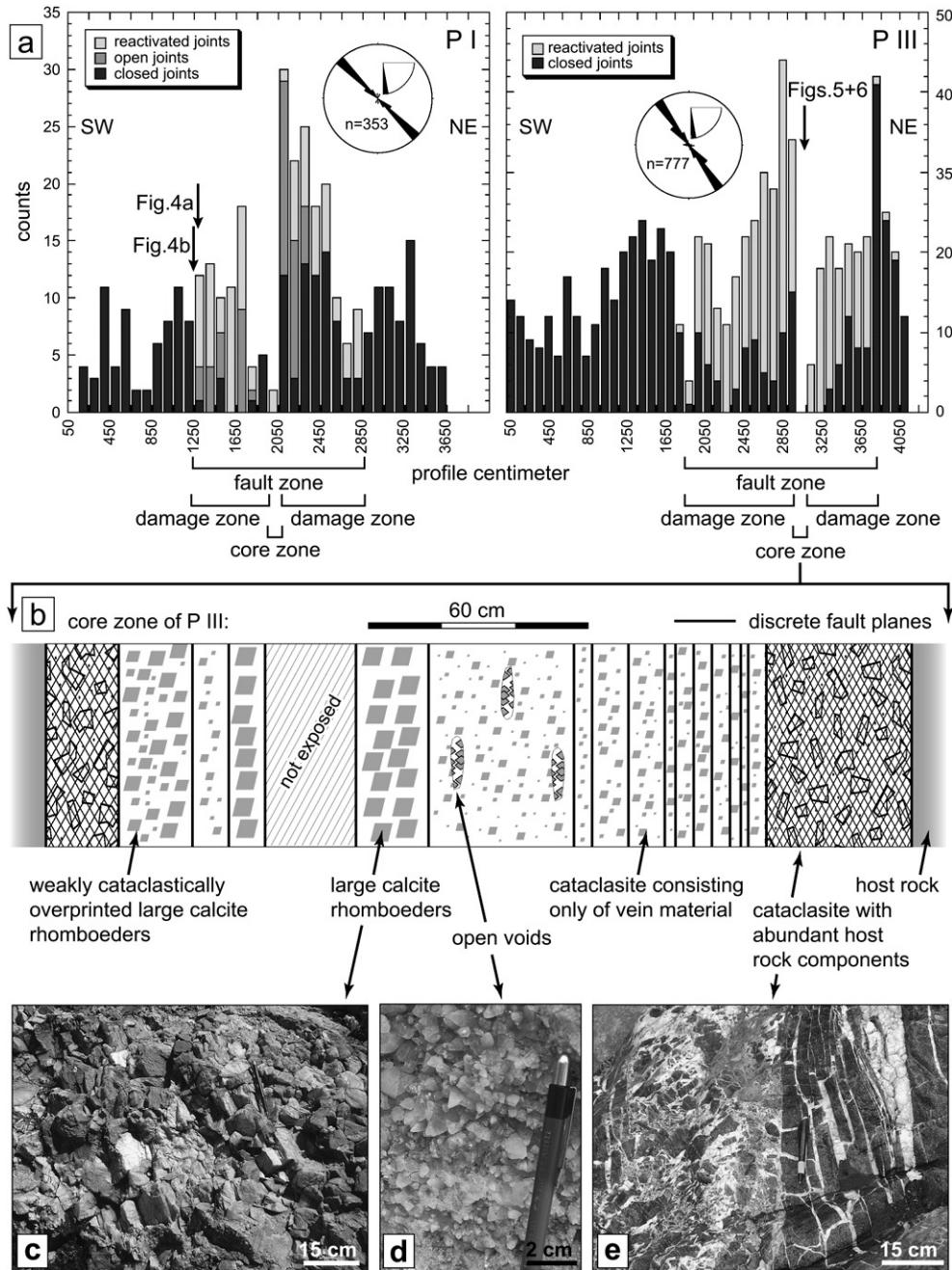
Fig. 3. (a) Joint distribution along profiles PI and PIII, profile locations are shown in Figs. 1 and 3. Rose diagrams show strike and dip angle of joints. (b) Profile across the core zone of PIII showing zones of different degrees of brittle overprint. (c) Calcite rhombohedrons with length of up to 10 cm indicate that large amounts of fluids have percolated through the fault zone. (d) Idiomorphic calcite crystals grown in open voids. (e) Incorporation of the carbonate host rock (dark grey) into the fault zone at the border of the damage zone indicated by the increasing proportion of white calcite material.

growth rims of the clasts and the differently sized matrix grains show scarce evidence for twinning (Fig. 6a). Thin and straight type I twins are observed at only a few locations (Fig. 6b). The lack of twinning indicates formation temperatures of <200 °C and very little deformation. The grain boundaries of matrix calcite grains are lobate (Fig. 6b), indicating grain boundary migration under the presence of fluids. However, cataclasite clasts in zone 2 are densely twinned and show thick, patchy twins with sutured boundaries, curved thick twins and twinned twins (Fig. 6a, c and d). These type IV and type III twins indicate intense deformation, dynamic recrystallisation and intracrystalline deformation mechanisms at temperatures above 250 °C and 200 °C, respectively. Twin boundary migration post-dating the twinning is observed in Fig. 6c and d. Calcite grains of zone 3 show only a few type I twins.

3.5. Isotope profile

Oxygen ($\delta^{18}O$) and carbon ($\delta^{13}C$) isotopic ratios were measured from a fault rock sample displaying macroscopic
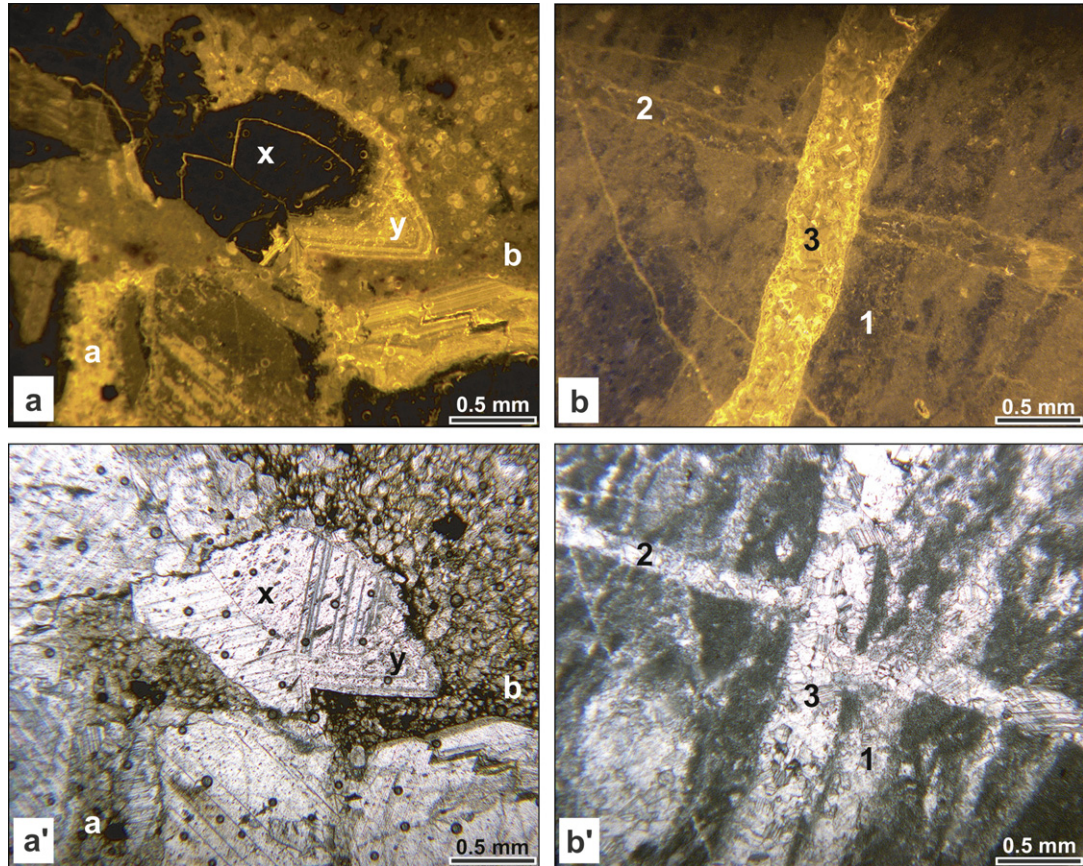
Fig. 4. Thin sections extracted from the fault zone (locations are shown in Fig. 3a). (a) Cathodoluminescence indicating different chemistry of vein material (*x* and *y*) and different generations of cataclasites (a, light and b, dark). (a′) The same section under plane polarized light. (b) Cathodoluminescence showing different fluid pulses in three different joint generations (1, oldest; 2, intermediate; and 3, youngest). (b′) The same section under plane polarized light.
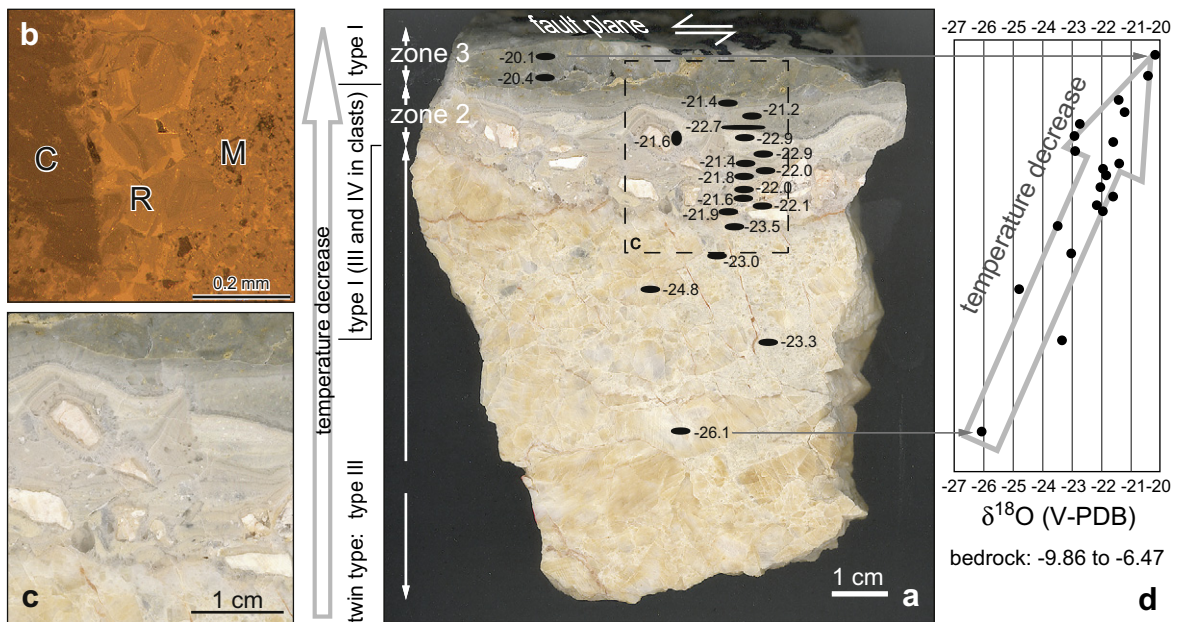

Fig. 5. Different observations made from one sample of Gemmi fault rock. (a) Zoned fault rock sample, the location of which is shown in Fig. 3. Note the three macroscopically different zones. Zoning of calcite twin types is indicated at the left of the picture. (b) CL-image of zone 2 illustrating different phases of fluid flow and brittle reactivation; M, fine-grained calcite matrix; R, old calcite core with newly grown crystal rim; C, cataclastic clast. (c) Magnification of layered zone 2, within which clasts of older cataclasite with rims of newly grown calcite crystals pervade a layered fine-grained calcite matrix. (d) $\delta^{18}O$-isotope profile across the three zones (locations of the measurements indicated in (a)).
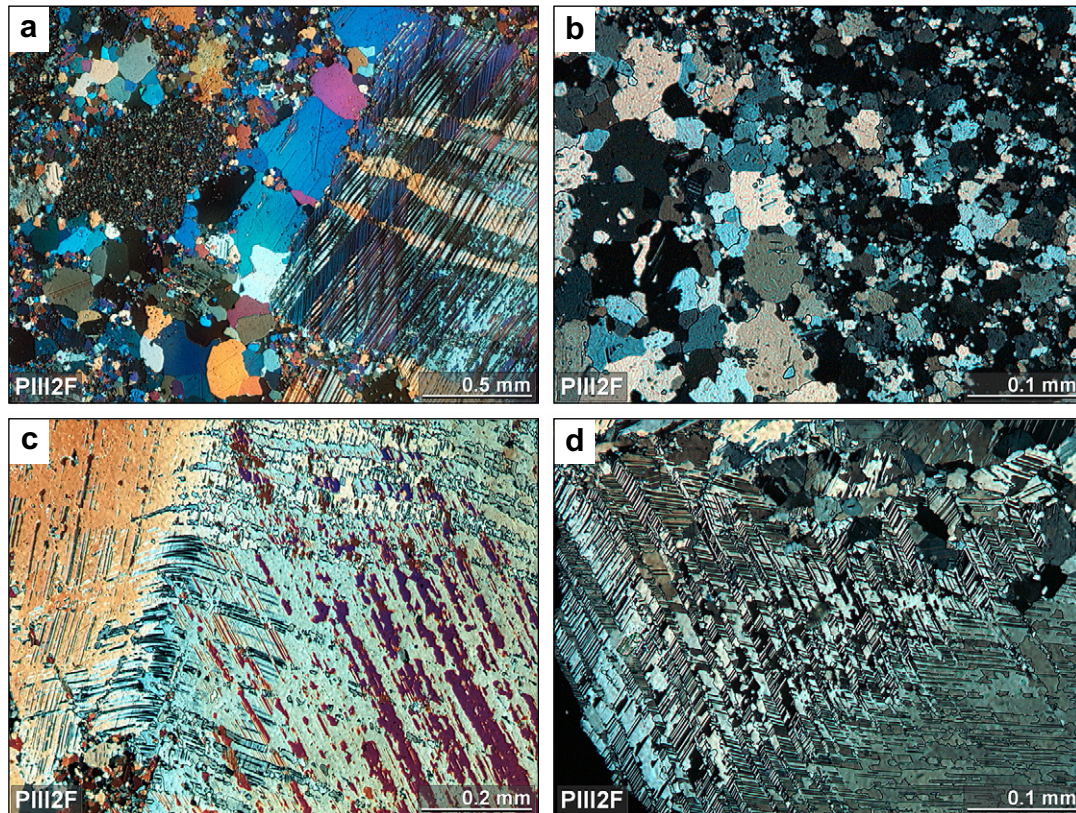
Fig. 6. Ultra thin sections of zone 2 cataclasite. (a) Example of a large clast (on the right) with a calcite rim in calcite matrix with different grain size. (b) Example of matrix grains showing lobate grain boundaries but no twinning. (c) Clast showing bent twins (twin type III) and twin boundary migration (twin type IV). (d) Clast showing twinned twins (twin type III) and sutured twin boundaries (twin type IV).

layering in the cataclasite (Fig. 5d). All calcite values are re-ported relative to V-PDB (Vienna Pee Dee Belemnite Stan-dard), the reproducibility of standard materials is ±0.08‰ (V-PDB). A short description of the methodological aspects of the isotope measurements is given in Appendix 1.1.

The carbon isotope ratios range from 0.62‰ to 0.96‰ V-PDB in zone 1, and from −0.07‰ to 0.16‰ V-PDB in zones 2 and 3. The oxygen isotope ratios decrease linearly with increasing distance from the fault plane from −20.08‰ to −26.11‰ V-PDB. A reference sample of the host rock lime-stone showed $\delta^{13}C$ values of 1.47‰ to 1.72‰ V-PDB and $\delta^{18}O$ values of −9.86‰ to −6.47‰ V-PDB.

4. Fault expression in Quaternary deposits

Quaternary sediments cover the fault at several locations. Rupture of the fault in post-glacial times would have disrupted the cover sediments providing evidence for recent fault activ-ity. In the western part of the Gemmi fault, a subtle indication for recent reactivation was discernible at the ground surface, where the fault trace crosses a slope covered by moraine scree (Fig. 2c) and displaces these young sediments. At another lo-cation along the fault a small ∼60 × 30 m depression in the limestone has been filled in with glacial and post-glacial sed-iments. A 3-D ground penetrating radar (GPR) survey was

undertaken over this small basin to investigate potential dis-ruption of the sediments (Fig. 2b). Results from the survey were used to identify an appropriate trench location, where the stratigraphic sequence could be investigated in more detail.

4.1. GPR data

A detailed description of the methodological aspects of the GPR-survey is given in Appendix 1.2. The processed data show a characteristically chaotic reflection pattern from the karstic limestone and more continuous, horizontal reflections from within the layered sediments (Fig. 7a). The chaotic pat-tern of reflections from the limestone precluded identification of the fault zone within the basement. A comprehensive anal-ysis of trace attributes, including reflection strength and in-stantaneous phase, identified subtle truncations of some of the horizontal reflections within the sediments that could be at-tributed to strands of the fault. After carefully interpreting cross-sections of the data volume we could not positively iden-tify fault displacement but could not discount past vertical movements on the order of <20 cm, the limit of the resolution of the data. The sharp contrast in reflection patterns between the bedrock and the young sediments allowed us to accurately determine the 3-D geometry of the basin revealing a deepening of the basin bottom to more than 4 m towards the north.
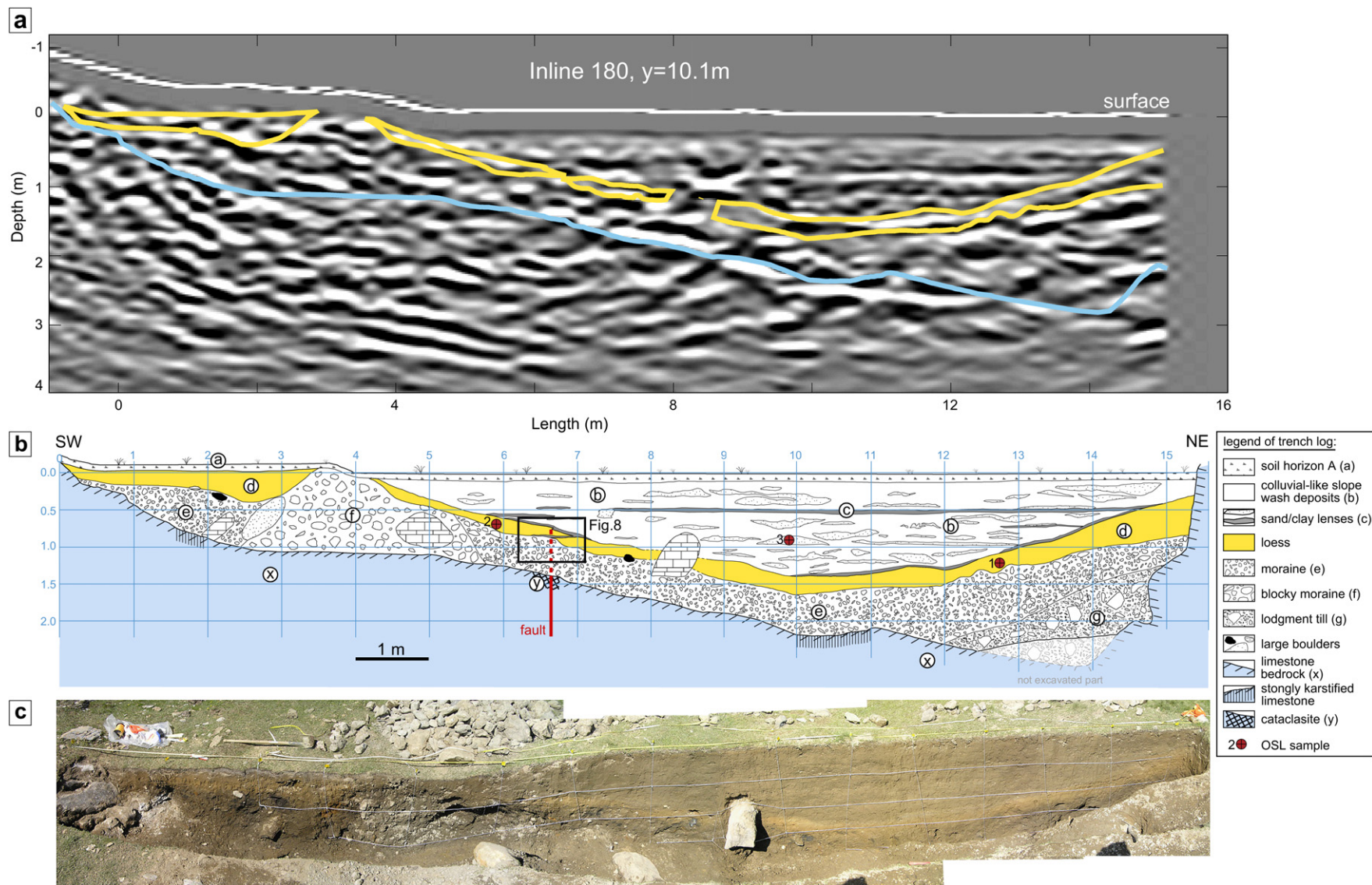
Fig. 7. (a) GPR cross section coincident with trench wall. (b) Trench log. The disrupted zone within the loess layer is shown in Fig. 8. (c) Photograph of trench wall.

4.2. Trench data

The Quaternary sediments were investigated in a large trench (15.4 m long and 2 m wide) that was excavated across the suspected fault (Figs. 1 and 2b). The trench site was selected in the narrowest part of the basin, where GPR data had revealed the limestone basement at a maximum depth of ~2 m, allowing us to reach the cataclasite beneath the sediments. The uncovered bedrock forms an asymmetric basin with a maximum depth of >2.2 m at the northeastern end of the trench (x in Fig. 7b). The near vertical bedrock wall on the northeastern side of the trench exhibits a steep-dipping to vertical polished fault plane.

The trench log in Fig. 7b and c illustrates the composition of the Quaternary sediments filling the depression. The base of the fill consists of a dark brown diamictic layer of up to 1.5 m in thickness. At the bottom, well-consolidated diamictic material (g in Fig. 7b) is overlain by weakly consolidated diamictic material (e and f in Fig. 7b). They both bear clasts with a variety of lithologies that are exotic to this area. We interpret these deposits as glacial sediments, i.e. basal till and reworked till, respectively. Large boulders of up to 1 m in diameter were found in the till material. These glacially transported blocks consist of limestone, sandstone and black shales. The larger blocks are imbricated and dip towards the southwest, indicating a northeast paleo-iceflow direction that originated from the nearby Wildstrubel glacier towards the northeast.

We interpreted a relatively constant 20–30 cm thick, fine-grained (silt to fine sand fraction), yellow layer deposited on top of the moraine (d in Fig. 7b) as a loess layer. It has a sharp upper contact, whereas the basal contact to the diamictic material is irregular. The loess layer mantles the underlying till unit.

An up to 1.5 m thick layer of grey-brown, colluvial-like slope-wash deposits overlays the yellow loess layer (b in Fig. 7b). It consists of brown fine-grained silt material intercalated with numerous sand and gravel lenses. We also observed thin (~5 cm), horizontal clay bands that extend for up to 7 m within this unit (c in Fig. 7b). These bands onlap the loess at both sides of the basin.

The uppermost 5–15 cm of the trench wall contains the top soil layer (a in Fig. 7b).

A cataclastic fault zone disrupts the partly karstified limestone bedrock from 6.4 m to 6.8 m. This 40 cm wide zone is split in the middle by an open joint or fault plane with a possible fault gouge filling. Neither striations on the fault planes nor vertical displacement of the bedrock surface were observed at this location.

In order to check for potential post-glacial activity at the fault, the unconsolidated sediments directly above the cataclastic bedrock were studied in detail. The ~50 cm thick moraine layer showed no evidence of deformation but small-scale disturbance within this very heterogeneous moraine material is difficult to detect. However, the otherwise continuous yellow loess layer is heavily disrupted at this location, incorporating moraine material from below. It displays flame-like structures

and the upper surface is vertically displaced by at least 5 cm across the disrupted zone (Fig. 8). We attribute most of these structures to fault movement because they occur over a short interval immediately above the cataclasite zone in the bedrock. Only the lower part of the overlaying slope-wash deposits are affected by the deformation. A continuous clay band approximately 30 cm above the loess sediment is not displaced (Fig. 8). We suggest that this layer was deposited some time after the last fault movement.

5. Age of faulting

5.1. Dating of veining and cataclastic overprint

In order to constrain the timing of the fault activity, we attempted to date the carbonate fault rock by Uranium–Thorium disequilibrium dating. Because of the vast difference in the solubility of U and Th, calcite precipitates from groundwater with negligible amounts of Th. The resulting disequilibrium in the Uranium decay series and subsequent *in situ* decay of ^{234}U to ^{230}Th can be used as a dating tool (Ivanovich et al., 1992). We measured five calcite samples from the fault rock sample of Fig. 5: two from zones 1 and 2 (samples taken
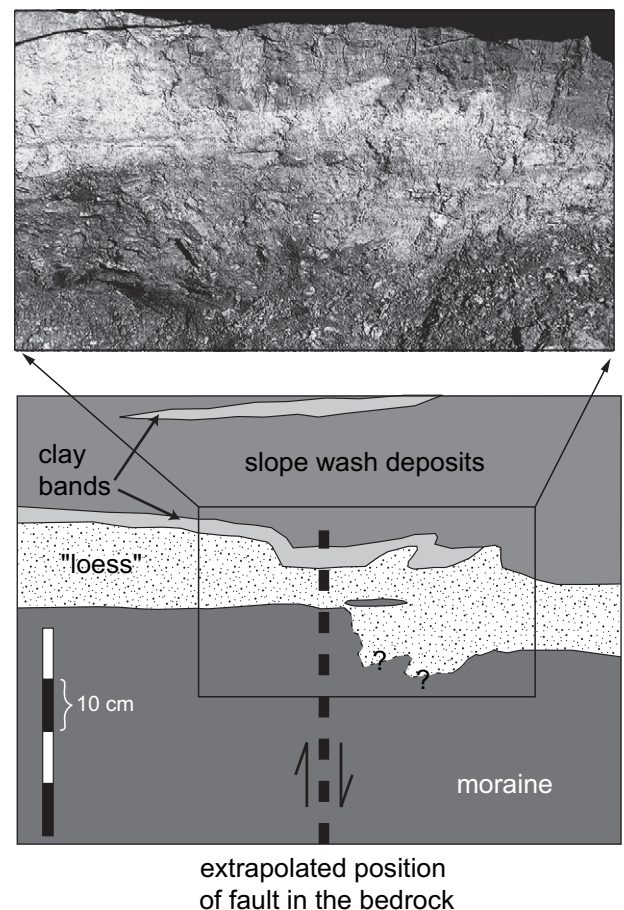

Fig. 8. Line drawing and close-up photograph of disrupted loess layer. Bold arrows show apparent offset.

from calcite rims), and one from zone 3. Samples were pre-screened using a Fujifilm BAS-1800 ß-scanner and areas of higher radioactivity were selected and sub-samples mechanically prepared using a hand-held diamond-wheel saw. Analytical procedures for the separation and concentration of U and Th were undertaken as described by Ivanovich and Harmon (1992). Isotopes of U (^{248}U, ^{238}U) and Th (^{230}Th, ^{232}Th) were measured separately on an Nu Instruments MC-ICPMS at the University of Bern, following the protocol described by Fleitmann et al. (2007). Results are summarized in Table 1.

The (^{230}Th/^{234}U) activity ratios fall between 0.999 and 1.131 (Table 1) and are all close to equilibrium, i.e. 1. The U–Th dating technique is based on the disequilibrium between ^{230}Th and ^{234}U at the time of formation of the mineral; equilibrium is re-established after some 500 kyr, forming the upper limit of this dating technique. The (^{230}Th/^{234}U) activity ratios reported here indicate that all the calcite material associated with the fault formed over 0.5 Ma ago.

However, some age information can be obtained from the ^{234}U/^{238}U values. Groundwater is characterised by (^{234}U/^{238}U) activity ratios greater than 1, most likely due to the preferential release of ^{234}U during weathering as a result of alpha recoil (Gascoyne, 1992). Secondary calcites, forming from these waters, therefore inherit their (^{234}U/^{238}U) activity ratio and these decay to unity with time. By ∼2.5 Ma secular equilibrium (where the rate of decay of each intermediate product equals the rate of its production) between ^{234}U and ^{238}U is reached, producing activity ratios of 1. The (^{234}U/^{238}U) activity ratios reported here, ranging from 1.0006 to 1.0782 (Table 1), i.e. above 1, thus broadly indicate an age of less than 2.5 Ma for the formation of the calcites.

If the original activity ratio is known or can be reconstructed, an age can be determined from the remaining excess of ^{234}U. Unfortunately, in this case, the initial (^{230}Th/^{234}U) activity ratios could not be measured or estimated, so no direct ages can be calculated. However, by combining information from the ^{230}Th/^{234}U and ^{234}U/^{238}U ratios, we can limit the time of formation of the cataclasite and the period of fluid flow to between 0.5 Ma and 2.5 Ma.

5.2. Dating of most recent fault activity

5.2.1. Pollen analysis

An analysis of pollen in the slope-wash material did not yield a result as the pollen content was too small and poorly preserved, prohibiting specific age determination. It is possible that the material was exposed at the surface for a long period, such leaving the pollen grains largely decomposed by microbial activity (R. Drescher-Schneider, Graz, Austria, personal communication).

5.2.2. Luminescence dating

The last daylight exposure of sediment grains, i.e. sediment deposition ages, can be determined from luminescence methods (cf. Aitken, 1998; Stokes, 1999; Preusser, 2004a; Lian and Roberts, 2006). The method analyses a light sensitive signal in quartz and feldspar grains that is erased during light exposure and rises during burial, when the grains are sealed from daylight. The signal is induced by the interaction of radioactive rays with the crystal lattice. To obtain accurate dates, the samples must be transferred to the laboratory without exposing them to light and all preparation and measurements should be carried out under low-energy red-light illumination. The amount of energy absorbed by the minerals is quantified in the laboratory by comparing the natural luminescence intensity of a sample with its response to known given doses (equivalent dose, De). In addition, it is necessary to measure the radioactivity of the sediment, and the luminescence age is then calculated as the ratio of De and dose rate (D) (the radioactive dose acting on the sample for a certain amount of time). Here, three samples from the Gemmi trench have been dated to further constrain the age of the observed fault deformation. Two samples (Gemmi1 and Gemmi2) were taken from the loess layer and one (Gemmi3) from the slope-wash deposits in the upper part of the sequence. For sample location in the trench see Fig. 7b.

A detailed description of the methodological aspects is given in Appendix 1.3.

A detailed list of data used for calculating luminescence ages is summarised in Table 2. IRSL ages of 13.5 ± 1.6 ka

Table 1

Uranium–thorium dating results, including concentrations in parts per billion of U and Th and isotopic ratios used in age determinations, i.e. ^{230}Th/^{234}U and ^{234}U/^{238}U

Sample (location)	U		Th		^{234}U/^{238}U[a]		^{230}Th/^{232}Th		^{230}Th/^{234}U[b]	
	ppb	±	ppb	±		±		±		±
MU 1 (zone 1)	65.1	0.1	21.84	0.10	1.0194	0.0020	9.72	0.12	1.060	0.012
MU 2 (zone 1)	65.1	0.1	15.18	0.07	1.0782	0.0014	15.77	0.19	1.131	0.012
MU 3 (zone 2)	1248.2	1.8	7.40	0.04	1.0006	0.0007	520.29	4.60	1.018	0.008
MU 4 (zone 2)	678.7	0.9	38.13	0.19	1.0107	0.0006	56.03	0.47	1.032	0.007
MU 5 (zone 3)	1871.6	2.5	100.71	0.33	1.0074	0.0006	56.46	0.40	0.999	0.006

Activity ratios were calculated using the decay constants described in Cheng et al. (2000). All three zones of the cataclasite were sampled; samples are numbered MU1 (Zone I, oldest) to MU5 (Zone III, youngest). The ^{230}Th/^{234}U ratios are close to equilibrium indicating the calcites formed over 0.5 Ma ago. The ^{234}U/^{238}U ratios, close to but not in equilibrium, indicate that none of the calcites are older than 2.5 Ma, thus constraining the period of their formation to between 0.5 Ma and 2.5 Ma.

[a] Measured activity ratio, (^{234}U/^{238}U) = (^{234}U/^{238}U)$_{ab}$/(λ^{238}U/λ^{234}U), where (^{234}U/^{238}U)$_{ab}$ is the abundance ratio of ^{234}U/^{238}U and λ^{238}U and λ^{234}U are the decay constants for ^{238}U and ^{234}U, respectively.

[b] Measured activity ratio, (^{230}Th/^{234}U) = (^{230}Th/^{234}U)$_{ab}$/(λ^{234}U/λ^{230}Th), where (^{230}Th/^{234}U)$_{ab}$ is the abundance ratio of ^{230}Th/^{234}U and λ^{234}U and λ^{230}Th are the decay constants for ^{234}U and ^{230}Th, respectively.

Table 2
Summary data of luminescence dating

Sample	Grain size (μm)	n	K (%)	Th (ppm)	U (ppm)	W (%)	Depth (m)	D_{cos} (mGy a^{-1})	D (Gy ka^{-1})	Recycling ratio	D_e (Gy)	Age (ka)
Gemmi1 (loess)	4–11	7	0.72±0.02	5.74±0.39	2.72±0.10	24.7	1.20±0.10	281±28	2.36±0.25	0.99±0.09	31.9±1.0	13.5±1.6
Gemmi2 (loess)	4–11	7	0.67±0.01	5.90±0.34	2.75±0.11	23.2	0.70±0.10	302±30	2.40±0.27	0.99±0.06	35.3±3.1	14.7±2.1
Gemmi3F (colluv.)	100–200	36	0.73±0.02	5.22±0.27	2.20±0.10	27.9	0.90±0.10	240±24	2.03±0.29	1.08±0.08	2.03±0.28	1.0±0.2
Gemmi3Q (colluv.)	100–200	31	0.73±0.02	5.22±0.27	2.20±0.10	27.9	0.90±0.10	240±24	1.53±0.26	1.05±0.09	3.67±0.43	2.4±0.5[a]

Given for each sample is the analysed grains size, number of measured aliquots (*n*), the concentration dose rate relevant elements (K, Th, U) with uncertainty resulting from scatter of values for different nuclides and general reproducibility of measurements as given by Preusser and Kasper (2001), present-day moisture content (*W*, given as percentage of the dry sample), cosmic dose rate with uncertainty (Dcos), total dose rate (*D*), the average recycling and fading ratio, equivalent dose (De) with standard error (see text for details) and resulting age estimate with standard deviation (1σ) colluv., Colluvial-like slope-wash deposits.

[a] Assuming that spread of individual De values is due to dose rate inhomogeneity gives a mean De of 13.3 ± 1.7 Gy and a resultant OSL age of 8.7 ± 2.0 ka.
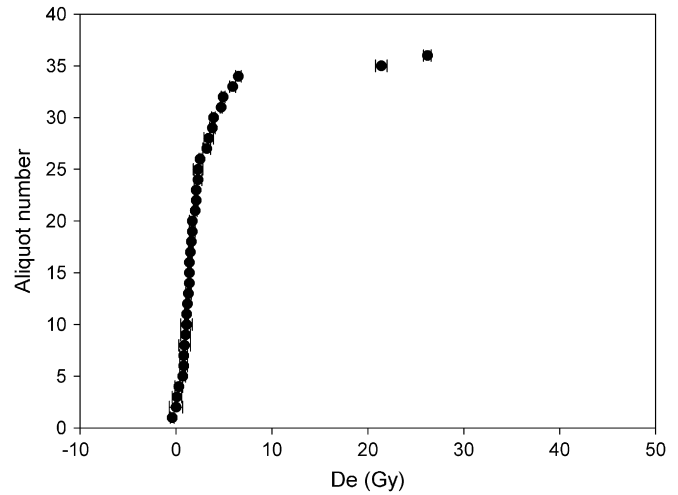

Fig. 9. Dose distribution plot for feldspar IRSL of sample Gemmi3.

(Gemmi1) and 14.7 ± 2.1 ka (Gemmi2) were determined for the two samples from the loess sediments. The aeolian nature of the sediment and the good performance of the measurement protocol imply that the two ages should be considered reliable and put the deposits of the loess sediments into the transition between the Last Glaciation of the Alps and the Holocene, i.e. into the Late Glacial period (cf. Preusser, 2004b).

The age of the samples from the slope-wash deposits (Gemmi3) is difficult to interpret. For the K-rich feldspar fraction, 34 of 36 aliquots gave D_e values between 0 Gy and 6.5 Gy (Gray) and only two values are above 20 Gy (Fig. 9). We consider these two values to represent outliers resulting from partial bleaching of IRSL prior to deposition and those are not considered in further calculations. The large scatter of the remaining 34 aliquots for very low D_e values can be explained by the low signal/background ratio of the IRSL signal. Mean D_e calculated from these values is 2.03 ± 0.28 Gy, which represents an IRSL age of 1.0 ± 0.2 ka.

For the quartz fraction an even larger spread of individual D_e is observed, with values ranging from 2.8 Gy to 41.0 Gy (Fig. 10). The source of this large spread of values is not clear.
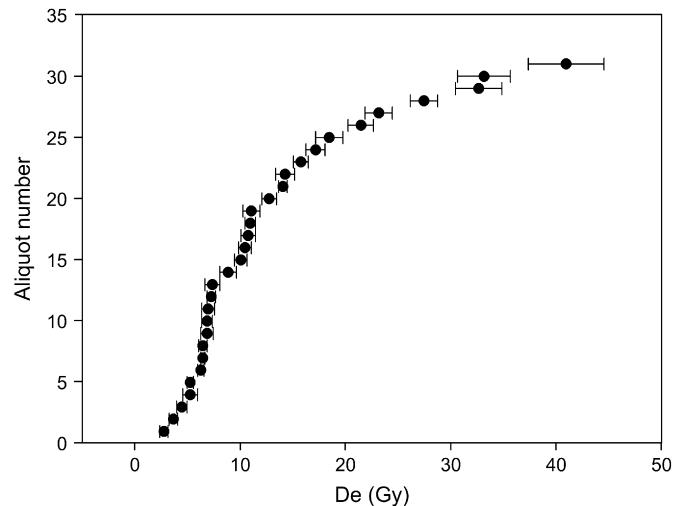

Fig. 10. Dose distribution plot for quartz OSL of sample Gemmi3.

The observed standard variation of 72% is much higher than values of about 20% due to dose rate inhomogeneity reported in the literature (cf. Preusser et al., 2007).

However, it is possible that the sediment under consideration here is highly inhomogeneous with respect to dose rate (e.g. the carbonate may have some hot spots of radioactivity). Using the mean D_e value of 13.3 ± 1.7 Gy of all measured aliquots gives an OSL age of 8.7 ± 2.0 ka. However, some influence of partial bleaching on the D_e distribution cannot be ruled out. Following Preusser et al. (2007) a mean D_e was calculated assuming a natural spread of individual D_e 20% values due to dose rate inhomogeneity. We obtained a mean value of 3.67 ± 0.43 Gy and an OSL age of 2.4 ± 0.5 ka. The likely age of deposition is therefore between 8.7 ± 2.0 ka and 2.4 ± 0.5 ka.

One problem remaining with the dating of sample Gemmi3 is the difference between feldspar IRSL and quartz OSL ages. The most likely explanation, underestimation of feldspar IRSL due to fading, is not supported by experimental evidence. Conversely, we did not find any indication for thermal transfer of quartz OSL, which would result in overestimated quartz ages. Nevertheless, we can conclude that the slope-wash deposits are of Holocene age and are most likely no older than a few thousand years (late Holocene).

6. Discussion and conclusion

Results from the many disciplines used in this study allow us to synthesize a history of the evolution of the Gemmi fault. The Gemmi fault was initiated as an open a–c-joint oriented perpendicular to the regional NE–SW trending fold axes at a late stage of Alpine nappe emplacement and related deformation. It belongs to a group of veins that are pervasive in the area of the Gemmi Pass, with extension directions parallel to the regional fold axes (Dietrich et al., 1983).

Exhumation rates of 0.83 mm/yr estimated from figure 10 in Herwegh and Pfiffner (2005) allow us to estimate that the exposed fault rock initially formed at about 8–12 km depth at around 10–15 Ma (Fig. 11). A similar exhumation rate for this area can be calculated using typical recent rock uplift rates of 1.2 mm/yr to 1.3 mm/yr (Kahle et al., 1997; in the sense of England and Molnar, 1990) and denudation rates between about 0.27 ± 0.14 mm/yr and 0.9 ± 0.3 mm/yr (Wittmann et al., in press; Norton et al., in press).

The Gemmi fault lies within a 20 m wide dense array of brittle joints oriented parallel to the major fault zone. We assume that with progressive strain, some of the joints interconnected to form a 0.5–3 m wide zone, which defines the core zone of the present-day fault. During this episode new parallel open joints formed and the contact between older vein filling and host rock partly opened. The bimodal distribution of joints in profile PIII (Fig. 3a) may indicate that a second ∼20 m wide zone of weakness SW of the main fault has not evolved into a fault zone. Considerable amounts of fluids percolated through the joints, precipitating idiomorphic calcite crystals and blocky calcite cement. As deformation concentrated in the core zone, strain and strain rates became high enough for the local formation of cataclasites. These fracturing and

calcite precipitation phenomena observed in the fault rock indicate dissolution–precipitation processes under the presence of fluids and brittle faulting.

The joint fill of the core zone was later overprinted by repeated brittle deformation. Several phases of fluid flow and brittle reactivation are registered in the fault rock, as indicated by different cathodo-microfacies at the micro-scale and by a zonation of the fault rock at the macro-scale. Differences in cathodo-microfacies occur either due to variations in saturation of the fluids (source-controlled) or due to deviations in pressure conditions (deformation-controlled). For example, a decrease in pressure caused by an increase in porosity may have led to precipitation.

The layering in zone 2 of the fault rock sample can be explained by a gravitational settling of fault gouge material in a dilative compartment of the fault zone. Small clasts of a more highly deformed cataclasite falling into this void formed a component-supported framework, in which fluid flow was possible. From these fluids calcite crystals grew idiomorphically and formed pendant calcite-crusts around the clasts. The fine-grained gouge material then settled in laminae, intercalated with thin layers of calcite crystals, which were precipitated during new fluid pulses.

As only proto-cataclasites occur in the fault rock, shear strain must have been limited. This is confirmed by the relatively low total displacement of about 10 m of the entire fault.

Temperatures during the early stage of faulting can be estimated from microstructures and twin types in the calcite cataclasite. Herwegh and Pfiffner (2005) report peak metamorphic conditions of 260–270 °C for a region encompassing the Gemmi fault. This is in close agreement with earlier temperature estimates of about 290 °C by Burkhard (1993). These values represent peak temperatures for the host rock of the Gemmi fault, which is in congruence with mylonitic textures and intense dynamic recrystallisation observed in the host rock limestone. Recent studies on carbonate mylonites of the Helvetic Alps have revealed that temperatures higher than ∼220 °C are required for dynamic recrystallisation in carbonate rocks (e.g. Herwegh and Pfiffner, 2005; Herwegh et al., 2005; Ebert, 2006).

Observations of the calcite twins indicate that, for the zoned fault rock, temperatures decreased towards the fault plane (Fig. 5a). Using the geothermometer of Burkhard (1993), which is based on the temperature-dependant occurrence of different types of calcite twins, the type III twins within the calcitic joint infill of zone 1 of the fault rock suggest temperatures of >200 °C.

However, type IV twins were found in the cataclastic clasts of zone 2, revealing temperatures of >250 °C. As no evidence for dynamic recrystallisation was found in the fault rock itself, these clasts must originate from a different, presumably older and more highly deformed cataclasite. The calcite grains of the matrix and the rims in zones 2 and 3 show scarce type I twins, which suggests temperatures <200 °C.

Using age constraints from the U–Th measurements of the zoned fault rock (0.5–2.5 Ma) and exhumation rates
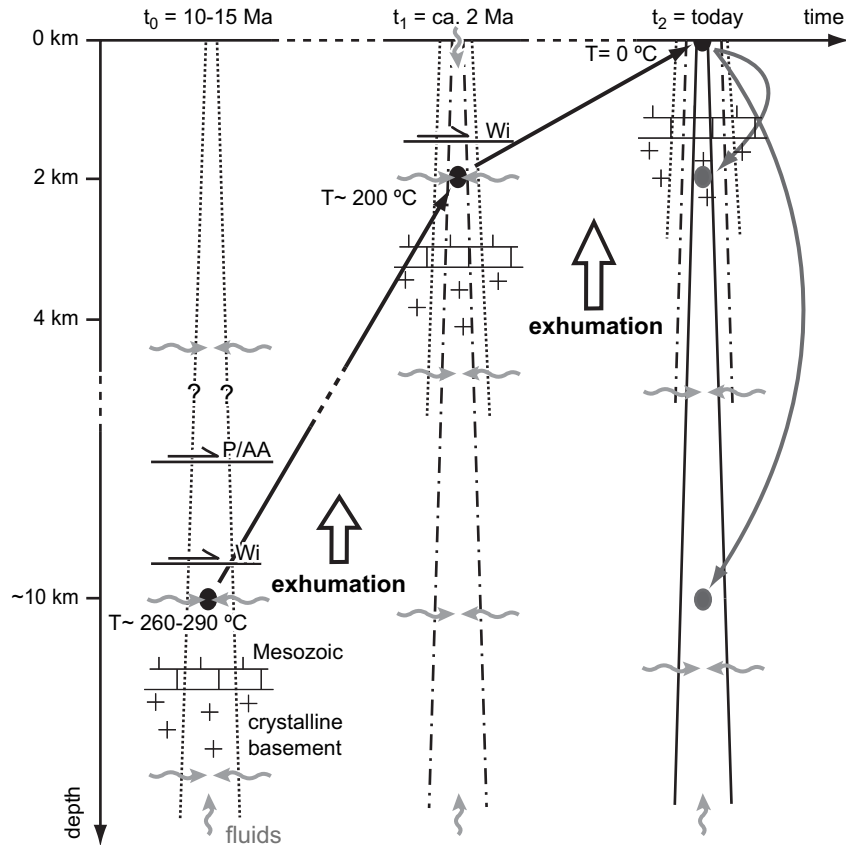
Fig. 11. Recapitulatory time–depth graph. Depths were calculated using exhumation rates derived from Herwegh and Pfiffner, 2005. Wi, wildhorn nappe; P/AA, penninic and austroalpine lid. Dark grey arrows point to areas of ongoing cycles of brittle deformation and fluid pulses in depth.

calculated from Herwegh and Pfiffner (2005), we can deduce that the 0.5–2.5 Ma old fault rock was ∼2 km beneath today's surface during its formation (Fig. 11). At this depth, strain rates and temperatures required for the formation of type III twins cannot be reached under normal conditions. Nevertheless, there are several possible sources of additional heat input. Firstly, episodic earthquake deformation and an additional input of shear heating could explain the formation of these twins. And secondly, hot hydrothermal fluids might have been present as indicated by recent hydrothermal springs in Leukerbad. These fluids may have raised the local geothermal gradient both vertically and laterally within the host rock.

The $\delta^{18}O$ values measured from the zoned fault rock sample show very low values (−26.11‰ to −20.08‰ V-PDB). In contrast, the bedrock carbonates have typical values for marine limestone of −9.86‰ to −6.47‰ V-PDB (Hoefs, 1997). Thus, they can be excluded as the primary source of fluids in the fault rock. More likely is the influence of either meteoric water, which has very negative values between −25‰ and −69‰ $\delta^{18}O$ V-PDB (i.e. 5‰ and −40‰ $\delta^{18}O$ SMOW, Hoefs, 1997) or fluids from granitic rocks, which have typical values between −35‰ and −16‰ $\delta^{18}O$ V-PDB (i.e. −5‰ to 14‰ $\delta^{18}O$ SMOW, Hoefs, 1997).

Recent weathering has not changed the original isotope trend as indicated by the values of the samples of zone 3. These are still higher than those of zone 1, although zone 3 was located

closer to the present-day surface and therefore should have more negative values if weathering had played a major role.

A significant trend in the $\delta^{18}O$ signal of the fault rock from lower values in zone 1 to higher values in zone 3 is observed. This trend represents either the weaker influence of fluids with negative $\delta^{18}O$ values towards the fault plane, or a temperature decrease. We prefer the latter interpretation because it is consistent with the afore mentioned calcite twin observations (Fig. 5a and d).

Burkhard and Kerrich (1988) and Dietrich et al. (1983) studied stable isotope data of veins and faults of the Helvetic nappes. Most of these show equilibrium values between vein and the host rock. Only two samples from Burkhard and Kerrich (1988) — a late tensile vein perpendicular to the fold axes and a large late normal fault — show negative $\delta^{18}O$ values comparable to those from our Gemmi fault, which would point to an external fluid source.

The Uranium-series isotopic ratios also provide some insight into the source of the fluids from which the calcitic fault rock formed. A distinct difference exists in the U-concentrations between the samples of zone 1, and zones 2 and 3 (Table 1). Zone 1 has a much lower U-concentration of 65.1 ppb, while the other two zones record substantially higher U-concentrations of 678.7 ppb and 1871.6 ppb, respectively. This difference indicates different fluid sources for the successive generations of calcite precipitation.

A similar example of a fault bounded hydrothermally mineralized breccia with a multistage deformation history is reported by Hofmann et al. (2004) from the Grimsel area, about 60 km to the ENE of the Gemmi Pass. Unlike the Gemmi fault examined in our study, this fault is located in crystalline rocks of the Aar massif. The breccia shows remarkably similar fluid flow indicators, crystal precipitation and brittle reactivation features. ^{39}Ar/^{40}Ar dating provides a middle Pliocene (3.30 ± 0.06 Ma) age of formation of the fault breccia. This age is similar to the 0.5 and 2.5 Ma age range for the mineralization of the Gemmi fault reported here.

In a trench excavated across the Gemmi fault we found deformed post-glacial sediments directly above cataclasite fault rock formed within limestone basement. A purely cryogenetic cause for these deformation structures can be ruled out for the following reasons. First, the vertical displacement of the loess occurs only above the fault zone. Second, the displacement of the loess layer can be followed continuously along the strike of the fault and over a distance of 2.5 m across the trench. And third, small water influxes were observed at several places along the floor of the trench but not from the fault zone cataclasite. Therefore, any seasonal freeze-thaw deformation is more likely to have occurred away from the fault zone.

Instead, we argue that the observations of deformed Holocene sediments in the trench indicate a post-glacial reactivation of the fault. The small vertical displacement and the rather chaotic deformation structures suggest strike-slip movement along the fault, consistent with observations of pre-glacial fault displacement at other locations. The OSL dating of the disrupted loess layer and the partly disturbed slope-wash deposits constrain the age of the last fault rupture. Latest activity on the Gemmi fault occurred after the deposition of the loess layer (i.e. after the Late Glacial period). Parts of the colluvial-like slope-wash deposits are also deformed, indicating rupture during more recent times. OSL sample Gemmi3 was taken at the same level as the deformed slope-wash deposits. Thus its age (between 8.7 ± 2.0 ka and 2.4 ± 0.5 ka) can be taken as the upper limit for the last time of reactivation. We therefore conclude that the last prominent reactivation of the Gemmi fault most likely occurred during the late Holocene. This result should, despite a scarcity of evidence from past studies, encourage further investigation of other faults for evidence of recent activity. We suggest that the present lack of evidence is probably a consequence of several factors: high erosion rates in the Alps, human-induced modification of the landscape, and a paucity of dateable Quaternary deposits, without which the exact timing of fault movements cannot be determined.

The strike of the Gemmi fault and the observed displacement along the Gemmi fault correlate with the present-day stress field, which shows an NW−SE trending compressive σ_1-axis and an NE−SW extensive σ_3-axis (Kastrup, 2002; Kastrup et al., 2004). Furthermore, the Gemmi fault is located at the northeastern end of an elongated earthquake cluster in the Valais north of the Rhône river in the Wildhorn−Rawil−Martigny area, which is directly to the west of this study area (Maurer and Deichmann, 1995; Maurer et al., 1997;

Deichmann et al., 2002). Analyses of focal mechanisms of earthquakes that occurred between 1961 and 1998 (Kastrup et al., 2004) show the predominance of strike-slip earthquakes and reveal two main strike orientations of possibly seismogenic faults in the area of the Rawil depression: NE−SW and NW−SE. Therefore, NW−SE trending faults like the Gemmi fault are prone to reactivation in today's stress field.

Using correlations between moment magnitude and surface rupture length, between maximum displacement and surface rupture length (after Wells and Coppersmith, 1994) and assuming a rupture over the complete length of the Gemmi fault (2.6−3.6 km), we estimate that the Gemmi fault experienced maximum magnitudes of 5.5−5.8, and displacements of 2−5 cm. These values are plausible in the context of the historical earthquake catalogue of Switzerland, where the two largest historically recorded earthquakes in the Valais had moment magnitudes of 6.4 (1524 at Ardon and 1855 at Visp, Earthquake Catalogue of Switzerland[1]).

The Gemmi fault has been active since its formation during Alpine nappe emplacement. Thus, from a single outcrop we can compare active and ancient deformation processes occurring at shallow and intermediate depth, a rare opportunity in the geological record. We suggest that the episodic cycles of brittle deformation and fluid pulses that formed the veins and cataclasites, i.e. the older structures presently exposed at surface, were ongoing at a few kilometers depth during the time of post-glacial fault activity. Given the regional seismicity pattern together with evidence for Holocene and historical activity, we conclude that episodes of veining and cataclasite formation are still occurring at depth within the crystalline basement (Fig. 11). At depth, structures similar to those observed at the Grimsel Pass (Hofmann et al., 2004) are likely to form now. In this way, the Gemmi fault provides a window through geological space and time.

---

[1] Swiss Seismological Service, 2002. ECOS − Earthquake Catalog of Switzerland. ECOS Report to PEGASOS, Version 31. 3. 2002. SED, Zürich. http://histserver.ethz.ch.

the preparation of the U–Th samples and Jan Kramers for the U-series discussion.

We thank J.P. McCalpin for his challenging review and an anonymous reviewer for the detailed comments, which improved the clarity and quality of the manuscript.

Appendix 1. Methodological aspects of the different techniques

1.1. Isotope measurements

Samples (0.2–0.5 mg) for the stable isotope analysis were drilled with a 0.5 mm diameter conical dentist drill. $\delta^{18}O$ and $\delta^{13}C$ isotopic compositions were measured using a VG Isocarb system attached to a VG Prism II isotope mass spectrometer at the Institute of Geological Sciences of the University of Bern. The phosphoric acid extraction was made at 90 °C.

1.2. GPR measurements

A Sensors and Software PulsEKKO GPR unit integrated with a self-tracking laser theodolite (Lehmann and Green, 1999) was used to survey the surface area of the basin (Fig. 2b). Stacked radar data were acquired on a dense (18 × 18 cm) grid over the depression using 0.5-m offset 200 MHz antennas. From additional common-midpoint (CMP) surveys we could determine a representative velocity for the subsurface sediments of 0.063 m/ns. The scaled and bandpass filtered data revealed reflections from both the sediment and the limestone basement to depths of ∼5 m. Processing included topographic migration, which was required to collapse diffractions and reposition dipping reflectors while accounting for topographic gradients within the survey area (Lehmann and Green, 2000). A top mute was used to mask the air- and ground-waves.

1.3. Luminescence dating

All samples were extracted by forcing opaque plastic tubes into the sediment, which were removed and sealed in light-proof bags. The outer part of the sediment core was removed in the laboratory to ensure that none of the material could have been exposed to light during sampling. Some portion of the inner part was used for preparation and was chemically pretreated (20% HCl, 30% H_2O_2) to remove carbonates and organic matter. For samples Gemmi1 and Gemmi2, the fine grain fraction 4–11 μm of the suspension was enriched by settling using Stokes' law. A solution of ∼2 mg sediment per 1 ml acetone was then pipetted on a stainless steal disc and the sample material settled on the disc after evaporation of the acetone. For sample Gemmi3, which is much coarser, the fraction 100–200 μm was collected by sieving and a quartz and a K-feldspar fraction, respectively, were separated using heavy liquids (sodium polytungstate solutions with densities of 2.70 g cm^3 and 2.58 g cm^3). The quartz fraction was additionally treated by etching for 40 min in 40% HF to remove any remaining feldspar contamination and the outer part of the quartz grains, which is effected by alpha irradiation.

All luminescence measurements were carried out on an automated TL/OSL-DA20 reader by Risø National Laboratory at the Institute of Geological Sciences of the University of Bern. Infrared stimulated luminescence (IRSL) of polymineral fine grains and K-feldspar separates were measured at 50 °C using a combination of Schott BG39 and L.O.T. Oriel Interference detection filter (410 nm). For the quartz separates, optically stimulated luminescence (OSL) by blue diodes was detected using a Hoya U340 filter. The purity of quartz samples was confirmed by measuring the response of the sample to IR stimulation and all quartz OSL measurements were carried out at 125 °C. The luminescence intensity of the samples is generally low (Fig. A.1).

For all measurements, the single-aliquot regenerative dose (SAR) protocol has been used (cf. Murray and Wintle, 2000; Wallinga et al., 2000; Preusser, 2003). Prior to dating a series of experiments was carried out to test the suitability of the measured material and verify the measurement parameters. A common feature observed for quartz that has a relatively young sedimentary history is thermal transfer of the luminescence signal caused by pre-heating the mineral after laboratory irradiation (Rhodes and Bailey, 1997; Rhodes, 2000; Preusser et al., 2006). We tested this for the Gemmi3 quartz sample (Gemmi3Q in Table 2) but found no evidence for thermal transfer, similar to results from Alpine quartz from other areas (Klasen et al., 2006; Preusser et al., 2007). There is also no evidence for any thermal transfer in the polymineral fine grain samples. The quartz and feldspar/polymineral fine grains were preheated for 10 s at 230 °C and 290 °C, respectively. Dose recovery tests revealed that a known laboratory dose was recovered within the precision of the method (dose recovery test are within 10% of given dose). Storage tests (four weeks at room temperature) were carried out for samples Gemmi1 and Gemmi3F to test if the feldspars are affected
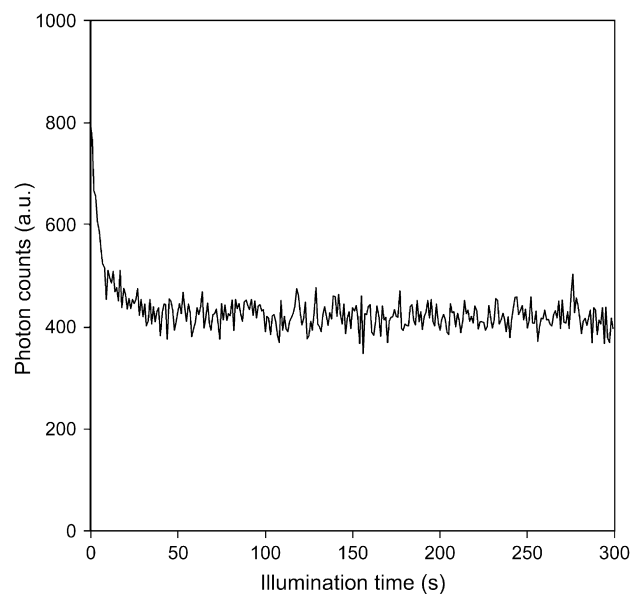

Fig. A.1. Example IRSL decay curve (Gemmi1) showing the predominantly low intensities of the samples.

by fading, which will result in underestimated ages (e.g. Walllinga et al., 2000; Auclair et al., 2003). These tests did not reveal any indication for fading of the investigated feldspars.

The concentration of dose rate relevant elements was determined in the laboratory by high-resolution gamma spectrometry (cf. Preusser and Kasper, 2001). No indication for radioactive disequilibria in the Uranium decay chain was observed (cf. Zander et al., 2007). In situ sediment moisture was used for dose rate calculation. The geological setting and the relatively young age of the sediment discount any major changes of the hydrological setting during residence time. The contribution of cosmic radiation to the total dose rate is estimated using present-day sample depth and considering the high elevation (2370 m) of the sample site (ADELE software).

References

Aitken, M.J., 1998. An Introduction to Optical Dating. University Press, Oxford.

Auclair, M., Lamothe, M., Huot, S., 2003. Measurement of anomalous fading for feldspar IRSL using SAR. Radiation Measurements 37, 487–492.

Baer, M., Deichmann, N., Braunmiller, J., Husen, S., Fäh, D., Giardini, D., Kästli, P., Kradolfer, U., Wiemer, S., 2005. Earthquakes in Switzerland and surrounding regions during 2004. Eclogae Geologicae Helvetiae 98, 407–418.

Burkhard, M., Kerrich, R., 1988. Fluid regimes in the deformation of the Helvetic nappes, Switzerland, as inferred from stable isotopes. Contributions to Mineralogy and Petrology 99, 416–429.

Burkhard, M., 1993. Calcite twins, their geometry, appearance and significance as stress–strain markers and indicators of tectonic regime: a review. Journal of Structural Geology 15, 351–368.

Calais, E., Nocquet, J.-M., Jouanne, F., Tardy, M., 2002. Current strain regime in the Western Alps from continuous Global Positioning System measurements, 1996–2001. Geology 30, 651–654.

Cheng, H., Edwards, R.L., Hoff, J., Gallup, C.D., Richards, D.A., Asmerom, Y., 2000. The half-lives of uranium-234 and thorium-230. Chemical Geology 169, 17–33.

Deichmann, N., Baer, M., Braunmiller, J., Ballarin Doflin, D., Bay, F., Bernardi, F., Delouis, B., Fäh, D., Gerstenberger, M., Giardini, D., Huber, S., Kradolfer, U., Maraine, S., Oprsal, I., Schibler, R., Schler, T., Sellami, S., Steimen, S., Wiemer, S., Wösser, J., Wyss, A., 2002. Earthquakes in Switzerland and surrounding regions during 2001. Eclogae Geologicae Helvetiae 95, 249–261.

Deichmann, N., Baer, M., Braunmiller, J., Fäh, D., Giardini, D., Kästli, P., Kradolfer, U., Wiemer, S., 2006. Earthquakes in Switzerland and surrounding regions during 2005. Eclogae Geologicae Helvetiae 99, 443–452.

Delacou, B., Deichmann, N., Sue, C., Thouvenot, F., Champagnac, J.-D., Burkhard, M., 2005. Active strike-slip faulting in the Chablais area (NW Alps) from earthquake focal mechanisms and relative locations. Eclogae Geologicae Helvetiae 98, 189–199.

Dietrich, D., McKenzie, J.A., Song, H., 1983. Origin of calcite syntectonic veins as determined from carbon-isotope ratios. Geology 11, 547–551.

Ebert, A., 2006. Microfabric evolution in pure and impure carbonate mylonites and their role for strain localization in large-scale shear zones. Ph.D. thesis, University of Bern.

Eckardt, P., Funk, H., Labhart, T., 1983. Postglaziale Krustenbewegungen an der Rhein-Rhone-Linie. Mesuration, Photogrammétrie. Génie rural 2, 43–56.

England, P., Molnar, P., 1990. Surface uplift, uplift of rocks, and exhumation of rocks. Geology 18, 1173–1177.

Escher, A., Hunziker, J.C., Marthaler, M., Masson, H., Sartori, M., Steck, A., 1997. Geologic framework and structural evolution of the Western Swiss-Italian Alps. In: Pfiffner, A.O., Lehner, P., Heitzmann, P., Müller, S.,

Steck, A. (Eds.), Results of NRP 20: Deep Structure of the Swiss Alps. Birkhäuser Verlag, Basel, pp. 205–221.

Fleitmann, D., Burns, S.J., Mangini, A., Mudelsee, M., Kramers, J.D., Villa, I., Neff, U., Al-Subbary, A.A., Buettner, A., Hippler, D., Matter, A., 2007. Holocene ITCZ and Indian monsoon dynamics recorded in stalagmites from Oman and Yemen (Socotra). Quaternary Science Reviews 26, 170–188.

Funk, H., Gubler, E., 1980. Höhenänderungen der Fixpunkte im Gotthard-Bahntunnel zwischen 1917 und 1977 und ihre Beziehung zur Geologie. Eclogae Geologicae Helvetiae 73, 583–592.

Furrer, H., Badoux, H., Huber, K., von Tavel, H., 1956. Geologischer Atlas der Schweiz. Blatt 32, 1267 Gemmi, scale 1, 25,000.

Furrer, H., Hügi, T., 1952. Telemagmatischer Gang im Nummulitenkalk beim Trubeln westlich Leukerbad (Kanton Wallis). Eclogae Geologicae Helvetiae 45, 41–51.

Gascoyne, M., 1992. Geochemistry of the actinides and their daughters. In: Ivanovich, M., Harmon, R.S. (Eds.), Uranium Series Disequilibrium: Applications to Earth, Marine and Environmental Sciences. Claredon, Oxford, pp. 34–61.

Gubler, E., Kahle, H.-G., Klingele, E., Mueller, S., Olivier, R., 1981. Recent crustal movements in Switzerland and their geophysical interpretations. Tectonophysics 71, 125–152.

Herwegh, M., Pfiffner, O.A., 2005. Tectono-metamorphic evolution of a nappe stack: a case study of the Swiss Alps. Tectonophysics 404, 55–76.

Herwegh, M., de Bresser, J.H.P., ter Heege, J., 2005. Combining natural microstructures with composite flow laws: an improved approach for the extrapolation of lab data to nature. Journal of Structural Geology 27, 503–521.

Hoefs, J., 1997. Stable Isotope Geochemistry, fourth ed. Springer Verlag, Berlin.

Hofmann, B.A., Helfer, M., Diamond, L.W., Villa, I.M., Frei, R., Eikenberg, J., 2004. Topography-driven hydrothermal breccia mineralization of Pliocene age at Grimsel Pass, Aar massif, Central Swiss Alps. Swiss Bulletin of Mineralogy and Petrology 84, 271–302.

Huon, S., Burkhard, M., Hunziker, J.C., 1994. Mineralogical, K-Ar, stable and Sr isotope systematics of K-white micas during very low-grade metamorphism of limestones (Helvetic nappes, western Switzerland). Chemical Geology (Isotope Geoscience Section) 113, 347–376.

Ivanovich, M., Harmon, R.S., 1992. Uranium Series Disequilibrium: Applications to Earth, Marine and Environmental Sciences. Claredon, Oxford.

Ivanovich, M., Latham, A.G., Ku, T.-L., 1992–1992. Uranium-series disequilibrium applications in geochronology. In: Ivanovich, M., Harmon, R.S. (Eds.), Uranium Series Disequilibrium: Applications to Earth, Marine and Environmental Sciences. Claredon, Oxford, pp. 62–94.

Jäckli, H.C.A., 1965. Pleistocene glaciation of the Swiss Alps and signs of postglacial differential uplift. The Geological Society of America, Inc. Special paper 84, 153–157.

Klasen, N., Preusser, F., Fiebig, M., Blei, A., Radtke, U., 2006. Luminescence properties of glaciofluvial sediments from the Bavarian Alpine Foreland. Radiation Measurements 41, 866–870.

Kahle, H.-G., Geiger, B., Bürki, B., Gubler, E., Marti, U., Wirth, M., Rothacher, M., Gurtner, W., Beutler, G., Bauersima, I., Pfiffner, O.A., 1997. Recent crustal movements, geoid and density distribution: contribution from integrated satellite and terrestrial measurements. In: Pfiffner, A.O., Lehner, P., Heitzmann, P., Müller, S., Steck, A. (Eds.), Deep Structure of the Swiss Alps: Results of NRP 20. Birkhäuser Verlag, Basel, pp. 251–259.

Kastrup, U., 2002. Seismotectonics and stress field variations in Switzerland. Ph.D. thesis, Swiss Federal Institute of Technology, Zürich.

Kastrup, U., Zoback, M.L., Deichmann, N., Evans, Keith F., Giardini, D., Michael, A.J., 2004. Stress field variations in the Swiss Alps and the northern Alpine foreland derived from inversion of fault plane solutions. Journal of Geophysical Research 109, doi:10.1029/2003JB002550.

Lehmann, F., Green, A.G., 1999. Semi-automated georadar acquisiton in three dimensions. Geophysics 64, 719–731.

Lehmann, F., Green, A.G., 2000. Topographic migration of georadar data: implications for acquisition and processing. Geophysics 65, 836–848.

Lian, O.B., Roberts, R.G., 2006. Dating the Quaternary: progress in luminescence dating of sediments. Quaternary Science Review 25, 2449–2468.

Maurer, H.R., Deichmann, N., 1995. Microearthquake cluster detection based on waveform similarities with an application to the western Swiss Alps. Geophysical Journal International 123, 588–600.

Maurer, H.R., Burkhard, M., Deichmann, N., Green, A.G., 1997. Active tectonism in the central Alps: contrasting stress regimes north and south of the Rhone Valley. Terra Nova 9, 91–94.

Muralt, R., Vuataz, F.-D., 1993. Emergence d'eau thermale et mélanges avec des eaux souterraines froides dans la gorge de la Dala à Leukerbad (Valais, Suisse). Bulletin du Centre d'hydrogéologie de l'Université de Neuchâtel 12, 111–135.

Murray, A.S., Wintle, A.G., 2000. Luminescence dating of quartz using an improved single-aliquot regenerative-dose protocol. Radiation Measurements 33, 57–73.

Norton, K.P., von Blanckenburg, F., Schlunegger, F., Schwab, M., Kubik, P.W., Cosmogenic nuclide-based investigation of spatial erosion and hillslope channel coupling in the transient foreland of the Swiss Alps. Geomorphology, in press. doi:10.1016/j.geomorph.2007.07.013.

Persaud, M., 2002. Active tectonics in the eastern Swiss Alps. Ph.D. thesis, University of Bern.

Persaud, M., Pfiffner, A.O., 2004. Active deformation in the eastern Swiss Alps: post-glacial faults, seismicity and surface uplift. Tectonophysics 385 (1–4), 59–84.

Pfiffner, O.A., 1993. The structure of the Helvetic nappes and its relation to the mechanical stratigraphy. Journal of Structural Geology 15, 511–521.

Pfiffner, A.O., Lehner, P., Heitzmann, P., Müller, S., Steck, A. (Eds.), 1997. Deep Structure of the Swiss Alps: Results of NRP 20. Birkhäuser Verlag, Basel.

Pfiffner, O.A., Schlunegger, F., Buiter, S.J.H., 2002. The Swiss Alps and their peripheral foreland basin: stratigraphic response to deep crustal processes. Tectonics 21, doi:10.1029/2000TC900039.

Preusser, F., 2003. IRSL dating of K-rich feldspars using the SAR protocol: comparison with independent age control. Ancient TL 21, 17–23.

Preusser, F., 2004a. Lumineszenzdatierung von Sedimenten als Beitrag zur Rekonstruktion der pleistozänen Klimageschichte des Alpenraums. Zeitschrift für Gletscherkunde und Glazialgeologie 38, 95–116.

Preusser, F., 2004b. Towards a chronology of the Late Pleistocene in the northern Alpine Foreland. Boreas 33, 195–210.

Preusser, F., Kasper, H.U., 2001. Comparison of dose rate determination using high-resolution gamma spectrometry and inductively coupled plasma-mass spectrometry. Ancient TL 19, 19–23.

Preusser, F., Ramseyer, K., Schlüchter, Ch., 2006. Characterisation of low luminescence intensity quartz from Westland, New Zealand. Radiation Measurements 41, 871–877.

Preusser, F., Blei, A., Graf, H.R., Schlüchter, Ch., 2007. Luminescence dating of Würmian (Weichselian) proglacial sediments from Switzerland: methodological aspects and stratigraphical conclusions. Boreas 36, 130–142.

Renner, F., 1982. Beiträge zur Gletschergeschichte des Gotthardgebietes und dendrochronologische Analysen an fossilen Hölzern. Physische Geographie 8, Zürich, Furrer, Keller, Gamper, Suter.

Rhodes, E.J., 2000. Observations of thermal transfer OSL signals in glacigenic quartz. Radiation Measurements 32, 595–602.

Rhodes, E.J., Bailey, R.M., 1997. The effect of thermal transfer on the zeroing of quartz from recent glaciofluvial sediments. Quaternary Science Reviews (Quaternary Geochronology) 16, 291–298.

Schlatter, A., Marti, U., 2002. Neues Landeshöhennetz der Schweiz LHN95. Vermessung, Photogrammetrie, Kulturtechnik 1, 13–17.

Schmid, S.M., Pfiffner, O.A., Froitzheim, N., Kissling, E., Schönborn, G., 1997. Integrated cross section and tectonic evolution of the Alps along the eastern transect. In: Pfiffner, A.O., Lehner, P., Heitzmann, P., Müller, S., Steck, A. (Eds.), Deep Structure of the Swiss Alps: Results of NRP 20. Birkhäuser Verlag, Basel, pp. 289–304. NFP20-Atlas: Deep Structure of the Swiss Alps.

Sue, C., 1998. Dynamique actuelle et récente des Alpes occidentales internes: approche structurale et sismologique. Ph.D. thesis, Université Joseph Fourier Grenoble.

Sue, C., Tricart, P., 2003. Neogene to ongoing normal faulting in the inner western Alps: a major evolution of the late Alpine tectonics. Tectonics 22, 5.1–5.25.

Stokes, S., 1999. Luminescence dating applications in geomorphological research. Geomorphology 29, 153–171.

Trümpy, R., 1998. Tectonic units of central Switzerland – their interpretation from A.D. 1708 to the present day. Bulletin of Applied Geology 3, 163–182.

Trümpy, R., 2003. Trying to understand Alpine sediments – before 1950. Earth-Science Reviews 61, 19–42.

Ustaszewski, M., 2007. Neotectonics in the central and western Swiss Alps. Ph.D. thesis, University of Bern.

Ustaszewski, M., Hampel, A., Pfiffner, O.A., Composite fault scarps in the Swiss Alps formed by the interplay of tectonics, gravitation and postglacial rebound: an integrated field and modelling study. Swiss Journal of Geosciences, 101, in press.

Ustaszewski, M., Pfiffner, O.A., Neotectonic Faulting, Uplift and Seismicity in the Central and Western Swiss Alps. In: Siegesmund, S., Fügenschuh, B., Froitzheim, N. (eds.). Tectonic aspects of the Alpine-Carpathian-Dinaride System. Geological Society, London, Special Publication, in press.

Wallinga, J., Murray, A.S., Wintle, A.G., 2000. The single-aliquot regenerative-dose (SAR) protocol applied to coarse-grain feldspar. Radiation Measurements 32, 529–533.

Wells, D.L., Coppersmith, K.J., 1994. New empirical realtionships among magnitude, rupture length, rupture width, rupture area, and surface displacement. Bulletin of the Seismological Society of America 84, 974–1002.

Wittmann, H., von Blanckenburg, F., Kruesmann, T., Norton, K.P., Kubik, P.W., The relation between rock uplift and denudation from cosmogenic nuclides in river sediment in the Central Alps of Switzerland. JGR Earth Surface, in press. doi:10.1029/2006JF000729.

Zander, A., Degering, D., Preusser, F., Brückner, H., 2007. Optically stimulated luminescence dating of sublittoral and intertidal sediments from the Emirate of Dubai, U.A.E. Quaternary Geochronology 2, 123–128.